Rheology of cellulose nanofibrils and silver nanowires for the development of screen-printed antibacterial surfaces

Hugo Spieser[a, b], *Alexandre Jardin*[a, c], *Davide Deganello*[b], *David Gethin*[b], *Julien Bras*[a,d], *Aurore Denneulin*[a, *]

[a] Univ. Grenoble Alpes, CNRS, Grenoble INP[e], LGP2, F-38000 Grenoble, France

[b] Welsh Centre for Printing and Coating, College of Engineering, Swansea University, Swansea, SA1 8EN, UK

[c] Université de Technologie de Troyes, 10004 Troyes CEDEX, France

[d] Nestle Research Centre, 1000 Lausanne, Switzerland

*** Corresponding author:**

Dr. Aurore Denneulin

Laboratory of Pulp and Paper Science and Graphic Arts

461 rue de la Papeterie

CS 10065 - 38402 Saint Martin d'Hères Cedex, FRANCE

aurore.denneulin@grenoble-inp.fr

+33 4 76 82 69 28

[e] Institute of Engineering Univ. Grenoble Alpes

Abstract: TEMPO (2,2,6,6-tetramethylpiperidine-N-oxyl)-oxidized cellulose nanofibrils (T-CNF) and silver nanowires (Ag NWs) were formulated as active inks. Their rheological properties were investigated to design optimal conditions for processing by the screen-printing process, with the aim of preparing antibacterial patterns. Rheological experiments mimicking the screen-printing process was applied to different ink formulations to investigate their thixotropic and viscosity properties. The experiments conducted at 1% wt total mass content and different ratios of T-CNF/Ag NWs, showed that the recovery (%), the recovery time and the viscosity are formulation dependent. A ratio 2:1 (T-CNF:Ag NWs) and total mass content of 2.5% wt was then selected to prepare an ink suitable for screen printing. Printing defects were corrected by addition of water-soluble polymer hydroxypropyl methylcellulose (HPMC). The selected formulation printed on flexible polyethylene terephthalate (PET) substrate displayed a 67.4% antibacterial activity against E. Coli in a standard contact active test, with a transparency superior to 70%, proving the promising features of the developed solution for active packaging applications.

Keywords: cellulose nanofibrils; silver nanowires; rheology; screen-printing; antibacterial activity.

1. Introduction

The packaging industry is facing new challenges in today's world and new innovations in packaging solutions have emerged such as active and intelligent packaging. Active packaging is usually defined as a technology able to respond to a stimulus either from the internal and external atmosphere of the packaging, by either releasing or adsorbing active substances. Several categories of active packaging can be distinguished such as gas scavengers, antioxidants or antibacterial packaging [1]. Antibacterial packaging is a common way to fight against bacterial contamination and so an interesting technique to enhance the shelf-life of packaged product especially for food applications.

Different active agents have been used for antibacterial packaging applications such as essential oils, organic acids, natural extract or nanoparticles. Silver nanoparticles (Ag NPs) demonstrate a strong antibacterial activity: its mode of action and the influence of different parameters on its activity have been thoroughly reviewed in the scientific literature [2]. Examples of Ag NPs activity against bacterial contamination in real food products have also been reported, against for instance cooked cereal or fruit [3, 4]. The use of Ag NPs or silver microparticles have been studied deeply in the field of printed electronics due to their high electronic and thermal conductivity properties. Notably the properties of silver nanoparticles with a high aspect ratio and rod-like aspect called silver nanowires have been studied because of their capability to form percolated networks [5]. Silver nanowires have also been studied for antibacterial applications adaptable to packaging applications and especially with polymeric substrate or composite such as polyethylene naphthalate (PEN) [6], polyvinyl alcohol (PVA) [7] or polypropylene/polytetrafluoroethylene systems (PP/ePTFE) [8], but also bio-based solution such as konjac glucomannan [9], chitosan [10] or PLA materials [11].

More recently, silver nanoparticles have been used in composites with cellulose and nanocellulose materials [12]. Composites with cellulose nanofibrils (CNF) present several

advantages such as to entrap the silver nanoparticles within the CNF network, to stabilize the Ag NPs and to control its dispersion as the produced systems are mainly prepared by in-situ Ag NPs synthesis [13, 14].

Because of the inherent activity of antibacterial packaging, active materials are mainly directly inserted inside or at the surface of the packaging film. For instance, using a coating or printing process to functionalize the surface of polymeric materials is an interesting way to produce antibacterial packaging by taking advantages of the versatility and flexibility of the deposition processes. Printing processes enable the deposition of a specific pattern when compared to surface deposition such as coatings. This localized deposition implies economy of materials and so the development of cost-effective solutions. Printing processes also enable the production of tailored solutions to a specific problem, and have been used in the field of active and intelligent packaging for the development of smart detectors, such as gas and humidity indicators/sensors and microbial sensors/indicators [15–18].

Only few references have reported the use of hybrid inks made of CNF and active materials for deposition by printing techniques. For instance, Koga et al. (2013) reported inkjet printing of TEMPO-oxidised CNF and carbon nanotubes for printed electronics applications [19]. Choi et al. (2016) also inkjet-printed CNF as a pre-layer on paper to improve the deposition of supercapacitors made of carbon nanotubes and a solid-state electrolyte. Another cellulosic substrate was used by Nechyporchuk et al. (2017), who printed regular pigment and silver nanoparticle conductive inks on cotton fabric [20]. Screen-printing was also used by El Baradai et al. (2015) to print a mixture of microfibrillated cellulose, graphite and carboxymethyl cellulose for the production of an electrode in lithium ion batteries [21]. Hoeng et al. (2017) reported the use of TEMPO-oxidised cellulose nanofibrils (T-CNF) and silver nanowires (Ag NWs) for printed electronics application [22]. The authors prepared inks fit for screen-printing requirement using the thickening characteristic and the shear-thinning properties of the T-CNF.

The ink optimization was based solely on the ink viscosity and the authors showed the need to add a water-soluble polymer named hydroxypropyl methylcellulose to modify the thixotropic and viscoelastic properties of the ink. No in-depths characterisation of the impact of the T-CNF/Ag NWs ratios and ink composition on the thixotropic behaviour of the inks were performed, and the study was mainly a proof of concept focused only on electrical properties. Cellulose nanofibrils in ink formulation are interesting due to their good properties as a dispersing agent, rheology modifier or film forming capability. Other examples using printing processes with cellulose nanofibrils mainly include 3D printing [23] or the use of nanocellulose materials as a substrate [24].

Printing processes include a wide range of techniques, the most common used for packaging applications being flexography, offset, gravure, screen and inkjet. Each process requires a specific ink behaviour, that needs to be tailored to fit the process requirement. Screen-printing is one of the most versatile printing techniques and consists of a squeegee pushing ink through a patterned screen mesh with open areas. Screen-printing is usually considered as easy to use, low cost and accepts a wide range of ink viscosity (around 1 to 200 $Pa.s^{-1}$), but does require shear-thinning behaviour and precise viscoelastic properties. CNF materials then present interesting rheological properties for such a process as they present strong shear thinning behaviour attributed to alignment of particles under shear and to the destruction of local entanglements (particle aggregates) [25]. This entangled network also promotes the thixotropic behaviour of CNF materials and appropriate viscoelastic properties [26]. TEMPO-oxidised CNF has met a strong interest since their development because of major energy savings during the mechanical fibrillated process and the low dimensions and highly charged particles that are produced [27]. The rheological properties of such materials are also deeply dependent on factors such as pH, electrolytes, surfactants, co-solvents, temperature or concentration [28–32]

The main challenges linked to antibacterial materials made of nanocellulose and silver nanoparticles are the materials preparation. In a large-volume and high standard application such as in the packaging field, versatility, control and up-scaling of the preparation processes are indeed key issues to address by the scientific community. Finally, the quality (homogeneity, transparency, etc) and antibacterial efficiency of the active packaging materials are of course major targets to achieve. This work is then dedicated on the investigation of the relation between the properties of nanocellulose/silver nanoparticles inks (and especially TEMPO-oxidised cellulose nanofibrils and silver nanowires) and their processability into antibacterial layers by the screen-printing process. The screen-printing process was selected because of its high versatility and flexibility. Several examples in the literature have reported the production of composite made of nanocellulose and silver nanoparticles, but to our knowledge, this work is the first example of printing a combination of cellulose nanofibrils and silver nanowires for the development of antibacterial surfaces. Only Martins et al. (2012) used a coating process to deposit a starch-based mixture of cellulose nanofibrils and silver nanoparticles on paper to develop an antibacterial substrate [33]. An investigation of the rheological properties of inks made of cellulose nanofibrils and silver nanoparticles have been reported by Hoeng et al. (2017) who did not fully investigate the impact of the component's ratios and mass content on the thixotropic properties of the suspensions [22].

In this work, the rheology properties of different formulations of TEMPO-oxidised cellulose nanofibrils and silver nanowires were quantified and evaluated with respect to the potential for use as ink in screen-printing. Different inks were first prepared at 1% wt total mass content and different ratios of T-CNF/Ag NWs. The thixotropic and viscosity properties of the inks were measured using a shear-induced rheological model, which mimics the screen-printing process. Higher mass content inks, as well as the influence of the hydroxypropyl methylcellulose (HPMC) additive, were also investigated. This optimization step led to the preparation of an

ink fit for screen-printing. Based on this, the influence of HPMC additives was assessed with respect to the topography of the print, print quality and the antibacterial activity of the produced pattern.

2. Materials and Methods

2.1. Materials

The materials comprise active inks as well as the substrate used for the preparation of the antibacterial layers, but also the different chemicals used in the characterization tests.

The active inks were prepared using TEMPO oxidised cellulose nanofibrils (T-CNF) and silver nanowires (Ag NWs). The aqueous suspension of T-CNF was provided by Betulium (Finland, CNF-A13, 5% wt, 1.63 ± 0.1 $mmol.g^{-1}$ measured charge density). The aqueous suspension of silver nanowires (Ag NWs) was purchased from NanoGap (USA) referenced under the tradename NGAP NF Ag-3170 (2.6% wt). The polyethylene terephthalate (PET) substrate used for the printing test was provided by Dupont (France) (Melinex® ST726 – 175 µm). Deionized water (DI water) was used for all experiments. Hydroxypropyl methylcellulose (HPMC) was also used in some inks formulation and was purchased from ThermoFisher Scientific (US) with the following specifications: 27.0-30.0% wt methoxy content and 7.0-12.0% wt hydroxypropoxy content. Hydrochloric acid (>99%) and sodium hydroxide (>99%) were acquired from Sigma Aldrich (US).

The following chemicals were used for the antibacterial tests: Escherichia Coli ATCC 8739 (Microbiologics, USA), L α-phosphatidyl choline (Sigma Aldrich, France, >99%), L-histidine (Roth, Germany, >98.5%), Tween®80 (Roth, Germany), potassium dihydrogen phosphate (Roth, Germany, >99%), sodium thiosulphate (Roth, Germany, >99%). The nutrient broth (NB, Roth, Germany) presents the following composition: 15 $g.l^{-1}$ peptone, 6 $g.l^{-1}$ sodium chloride, 3 $g.l^{-1}$ beef extract, 1$g.l^{-1}$ glucose. The plate counting agar (PCA, BD Difco, USA) presents the following composition: 15 $g.l^{-1}$ agar, 5 $g.l^{-1}$ peptone and 3 $g.l^{-1}$ beef extract. The materials were used as received. Isotonic solution (IS) was prepared by dissolving calcium chloride in DI water

at 8.5 $g.l^{-1}$. The neutralising solution was prepared by dissolving the following chemicals in 1 l of DI water: 3 g of L α-phosphatidyl choline, 1 g of L-histidine, 30 g of Tween®80, 10 g of potassium dihydrogen phosphate, 4.10^{-4} g of sodium thiosulphate and the pH was controlled between 7 and 7.2.

2.2. Raw material characterization

The work reported by Hoeng et al. (2017) showed how ultimately the T-CNF film provided a matrix within which the Ag NW's were dispersed and suspended [22]. Furthermore, viscosity of a particle laden fluid (such as T-CNF and Ag NWs suspensions) is influenced by the size and shape of any particle content [34, 35] and consequently determination of T-CNF and Ag NWs dimension is an important consideration.

To measure their morphological and dimensional parameters, the T-CNF were imaged by Transmission Electronic Microscope (TEM) on a CM 200 equipment from FEI/Phillips (Japan) with a TemCam F216 camera from TVIPS (Germany)[36]. To obtain distinct fibres, prior to imaging, the T-CNF was diluted, drop-casted on a copper grid and dyed with uranyl acetate. The acceleration voltage was set at 200 kV. The diameter and length of the T-CNF were measured by analysing the TEM images using the FIJI software [36–38]. Due to coloration and entanglement, measurements were complex to perform, however errors were managed through a suitable sample size of nanofibrils: 10 nanofibrils were measured on each image and the measurements were conducted on 10 different images. A representative example of the TEM images is provided in **Fig. 1**. The average and associated standard deviation are presented. The measured parameters for the T-CNF and the ones provided by the manufacturer for the Ag NWs are summarized in **Table 1**.

Table 1 *T-CNF and Ag NWs morphological parameters either measured or supplied by the manufacturer*

Materials	Length (nm)	Diameter (nm)	Average calculated aspect ratio	Oxidation charge (µmol.g^{-1})
T-CNF	297 ± 133	8 ± 4	37	1630 ± 93
Ag NWs	28 000 ± 23 000	72 ± 21	389	-

As the oxidation charge of T-CNF materials has a strong impact on the rheological parameters [39, 40], the charge density (mmol.g^{-1}) of the T-CNF was measured following a standard procedure. A suspension at approximately 250 mg.ml^{-1} was prepared and the pH was set to pH<3.5 with hydrochloric acid (0.1 mol.l^{-1}). After 15 min of magnetic stirring, the mixture was titrated with sodium hydroxide (0.01 mol.l^{-1}) by recording conductivity. Equivalent volumes were calculated by intersection of the linearly correlated curves: the first volume corresponds to the titration of the hydrochloric acid whereas the second corresponds to the titration of the T-CNF carboxylic acid function. Charge density (X) was calculated using the following equation (**1**):

$$X\ (mmol.g^{-1}) = \frac{C_{NaoH} \times V_{2eq}}{m} \quad \textbf{(1)}$$

Where X (mmol.g^{-1}) is the charge density, C_{NaOH} (mmol.l^{-1}) is the sodium hydroxide concentration, V_{2eq} (l) is the second equivalent volume corresponding to the carboxylic acid function titration volume and m (g) the dry mass of T-CNF titrated. Three titrations were conducted and the average is presented in **Table 1**.

The Ag NWs were imaged using a Field-Emission Gun Scanning Electron Microscope (FEG-SEM) apparatus (Ultra 55) from Zeist (France). A diluted suspension of Ag NWs was drop-casted on a SEM stub and left to dry overnight. The Ag NWs were then imaged after Gold/Palladium coating (2 nm) and using a 3kV accelerating voltage and 5.4 mm working distance. A representative example of the images is provided in **Fig. 1**.

a)

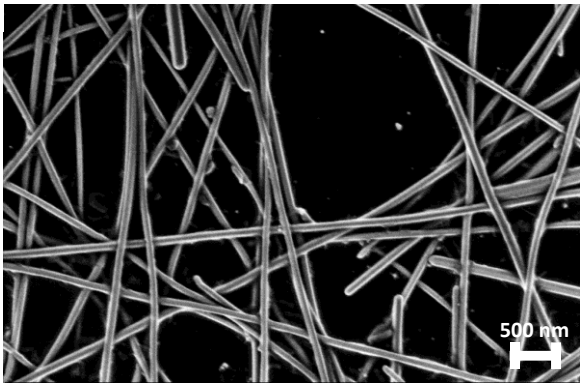

b)

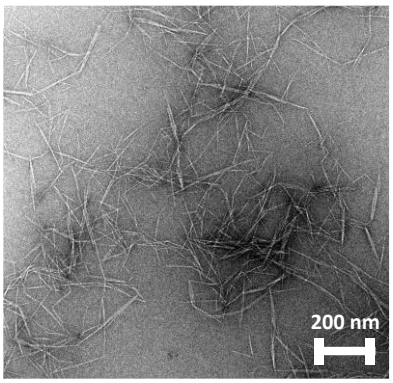

Fig. 1 *Electron microscopy of the raw materials with a) SEM-FEG of Ag NWs and b) TEM of T-CNF*

In order to achieve individual nanoparticles on a smooth surface, diluted suspensions of T-CNF and Ag NWs were also drop-coated on Mica, left to dry overnight and then imaged by Atomic Force Microscopy (AFM) using a Veeco NanoScope-V (Canada) microscope equipped with a OTESPA Bruker (USA) silicon cantilever. The images are available in the supplementary material (**Fig SI 1**).

To assess homogeneity, the turbidity of the T-CNF suspension (0.1% wt) was measured with a portable turbidimeter. During the measurement, the scattered light at 90° angle is compared to the incident light and the experiments were performed 6 times.

2.3. Inks preparation

All active inks prepared throughout this work were redispersed in water at the desired mass content and ratio between T-CNF and Ag NWs using an Ultra Turrax high shear disperser for 30 s at 10 000 rotation per minute (RPM), that is based on laboratory good practice experience (proper dispersion but no physical damage). Throughout this work, the ink concentration is mass concentration (% wt) and the solvent was DI water. Several inks with T-CNF mass content ranging from 0 to 1.66% wt and Ag NWs mass content ranging from 0 to 1% wt were prepared.

The inks based on T-CNF/Ag NWs (1.66% wt/0.83% wt) and HPMC additives (0, 3, 5 and 8% wt) were prepared with the following protocol: the desired mass of T-CNF and Ag NWs were weighed with the desired amount of water, and the desired mass of HPMC was added slowly at 60°C under several steps of high shear dispersion (30 s, 10 000 RPM) until the HPMC was uniformly dissolved. To simplify the notation in the following section, the inks will be named only after their HPMC content (0% HPMC, 3% HPMC, 5% HPMC or 8% HPMC).

2.4. Rheology and inks properties

All rheological tests were conducted on a MCR 302 rotational rheometer from Anton Paar (Germany). All the tests were performed at 20°C with a set gap of 0.108 mm and using a cone on plate geometry with the following characteristics: diameter of 50 mm, truncate of 55 µm and angle of 1.013°. Rheological events occurring during the screen-printing process was simulated using a protocol adapted from Neidert et al (2008) [41], where shear rates that are typical of those experienced during different stages of the process are applied. During a deposition process such as screen-printing, high shear is usually applied and the ink structure can thus be altered (network modification, change in the solid-liquid interaction, etc), and this is particularly true for inks composed of high aspect ratio nanoparticles. The thixotropic rheological component of

these inks needs to be determined to obtain the desired behaviour after deposition on the substrate. The first step simulates the ink at rest on the screen by applying a 2 s^{-1} shear rate for 150 s (step 1). The second step simulates the squeegee passing over the screen and transferring the ink to the substrate by applying a 1000 s^{-1} shear rate during 15 s (step 2). The last step simulates the ink at rest on the substrate after printing by applying a 2 s^{-1} shear rate for 150 s (step 3). The three-step rheological experiment was performed three times for the formulation at 1% wt total mass and was found to be highly reproducible. For economy of materials, the other formulations were then tested once.

Surface tension in conjunction with substrate specific surface energy is important in the consideration of substrate wetting and hence the surface tension of the prepared inks was evaluated using the Du Noüy ring method on a Sigma 700 tensiometer from Attension (UK) with at least 20 measurements on each suspension.

2.5. Screen-printing

The screen-printing experiments were conducted on a Dek Horizon 03i printer (ASM Pacific Technology, Singapore) with the following optimized parameters: 1 mm print gap, 120 $mm.s^{-1}$ forward speed, 80 $mm.s^{-1}$ reverse speed, and 7 kg squeegee load. The polyester screen mesh used presents the following specifications: 120 $thread.cm^{-1}$ mesh count, 34 µm thread diameter, 12 µm emulsion thickness and 45° screen angle. The resulting prints were dried at 120°C for 1 min in an oven and each formulation was printed at least 3 times to assess the reproducibility of the process. The quality of the print was quantified by scanning them in 8-bit grey scale on a black background and performing image analysis using the FIJI software. The grey level histogram distribution and the corresponding standard deviation could then be extracted using the software. For a straightforward representation, the histogram distributions were smoothed and drawn as curves.

2.6. Print surface characterisation

As parameters linked to the quality control of the deposition, the thickness (nm) and surface roughness (µm) of the deposited layer was measured on a Veeco Wyco NT9300 white light interferometer with the following parameters: 1.2 × 0.93 mm measured area, 736 × 480 pixels resolution, ×5 magnification. To measure the thickness, a specific focus was made on the edge area of the printed layer. The height difference between the substrate and the ink layer was measured by excluding the printing edge which can present irregularities. The average surface roughness (*Sa*) was measured on the whole scanned area. At least 5 measurements were taken on 3 different printed squares for each formulation.

The transparency of the printed pattern was investigated by measuring the transmittance at 550 nm wavelength on a UV-spectrophotometer (Shimadzu Manufacturing Inc., USA). At least 5 measurements were conducted on 3 different printed square for each sample.

2.7. Antibacterial properties

Prior to testing, the desired solutions, glassware and tools were sterilized in an autoclave for 20 min at 120°C/1.034 bar. The antibacterial properties of the screen-printed layers toward *E. Coli* bacteria were evaluated by performing the AATCC TM100-1998 standard [42] test. To summarize the technique, a bacterial suspension with a known concentration was deposited on the surface of the samples and the concentration was measured again after 24 hours of contact to assess the activity of the prints. For each sample, a 2 cm × 2 cm surface of the prints was cut and dry-sterilized at 60°C for 16 h in an oven prior to the experiments. *E. Coli* bacterial suspension was diluted at 5.10^5 CFU.ml^{-1} in 20% NB (1 volume NB, 4 volume IS) and 200 µl was drop-casted in microdroplets form on the surface of the sample. The systems were then incubated at 37°C for 24 h. The samples were then recovered, washed with 50 ml of the

neutralizing solution and the remaining bacterial concentration was measured by a plate counting method using plate counting agar. Antibacterial activity (AA, %) was calculated with the following equation (2):

$$AA\ (\%) = \frac{BC_{PET\ ref} - \mathrm{BC}_{print}}{BC_{PET\ ref}} \times 100 \quad \textbf{(2)}$$

Where $BC_{PET\ ref}$ (log CFU) is the bacterial concentration on PET substrate after 24 h of incubation, BC_{print} (Log CFU) the equivalent on the printed sample. 3 different samples were tested for each formulation and the average is presented with associated standard deviation.

3. Results and discussions

3.1. Rheological properties of raw materials

The morphological parameters of the supplied T-CNF were assessed by TEM microscopy. Their length was measured at 297 ± 133 nm and their diameter at 8 ± 4 nm, which is relatively small but similar to previous studies for T-CNF with high surface charge [35, 43]. The T-CNF suspension is highly homogeneous as indicated by its turbidity measured at 18.9 ± 1.8 NTU. The length and diameter of the Ag NWs are significantly higher, respectively 28 ± 23 µm and 72 ± 21 nm, as supplied by the manufacturer. This difference in dimensions can be seen on the TEM, SEM-FEG and AFM images (**Fig. 1** and **Fig. SI 1**). Different aqueous inks were prepared using the raw materials and their rheological parameters were then investigated.

For these primary experiments, the total mass content was fixed at 1% wt and ratios between the two components was varied between 0 and 1. The results are displayed in **Fig. 2** with the overview of the three steps (**Fig. 2a**) and a zoom on the step 3 (**Fig. 2b**).). The latter includes an associated curve that will be used to capture the recovery time consistently between samples. The individual step 3 and associated fitting for each formulation can be found in the supplementary material (**Fig. SI 2**).

a)

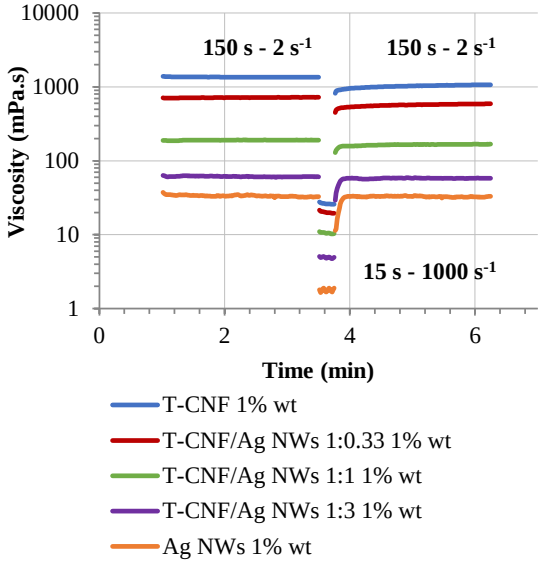

b)

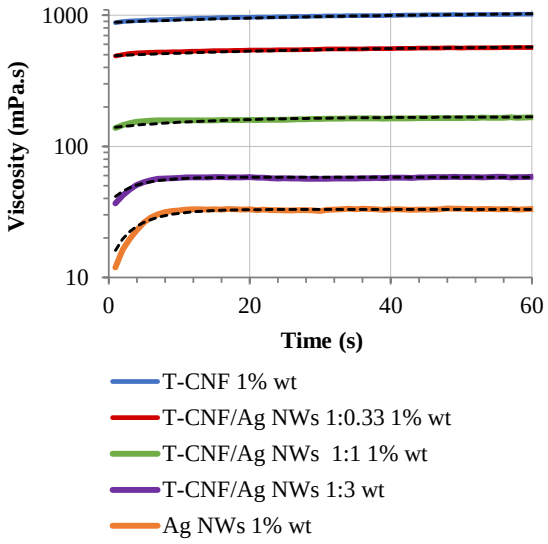

Fig. 2 *3-step rheological model of shear-induced deposition process for T-CNF/Ag NWs inks at 1% wt and ratios varying from 0 and 1 with a) overview of the viscosity vs time response and b) step 3 built-up curve and associate stretch exponential model (dotted lines)*

Different parameters (recovery time, recovery, viscosity) were extracted from this experimental data and are summarized in **Table 2**. The viscosity (step 1, step 2 or step 3) is the viscosity measured at the end of the corresponding step. The recovery (%) is the ratio of the viscosity at the end of step 1 and at the end of step 3 as calculated from equation **3**:

$$Recovery\ (\%) = 100 \times \frac{\eta_{end\ STEP\ 3}}{\eta_{end\ STEP\ 1}} \quad \textbf{(3)}$$

Where η_{end} STEP 1 (Pa.s) and η_{end} STEP 3 (Pa.s) are the viscosity at the end of steps 1 and 3 respectively. The recovery time (s) was estimated by fitting the viscosity recovery in step 3 to the first order stretched exponential model from equation **4,** as classically used to characterise the build-up recovery structure of thixotropic fluid, using the assumption that the recovery process is due to the re-orientation of the system during the transition steps [34, 44, 45].

$$\eta\ (Pa.s) = \eta_{\infty} + (\eta_0 - \eta_{\infty})(1 - e^{-\left(\frac{t}{\tau}\right)^r}) \quad \textbf{(4)}$$

Where η (Pa.s) is the viscosity, η_{∞} (Pa.s) the viscosity for an infinite shearing time, η_0 (Pa.s) the viscosity at the beginning of the shear step, t (s) is the time, τ (s) a time constant and r a constant (dimensionless). In the specific case of our study, the equation **4** was adapted to yield equation **5**:

$$\eta\ (Pa.s) = \eta_{end\ STEP\ 3} + (\eta_{start\ STEP\ 3} - \eta_{end\ STEP\ 3})(1 - e^{-\left(\frac{t}{\tau}\right)}) \quad \textbf{(5)}$$

Where η (Pa.s) is the viscosity, η_{end} STEP 3 (Pa.s) the viscosity at the end of the step 3, η_{start} STEP 3 (Pa.s) the viscosity at the start of the step 3 (taken 1 s after the switch from step 2 to step 3, to limit inertia interferences), t (s) is the time and τ (s) is the recovery time. The r constant was assumed to be equal to 1.

Table 2 Recovery time (s), recovery (%) and viscosity (mPa.s) extracted from the 3-step model, compared to the T-CNF content

	Ag NWs 1% wt	T-CNF/Ag NWs 1% wt 1:3	T-CNF/Ag NWs 1% wt 1:1	T-CNF/Ag NWs 1% wt 1:0.33	T-CNF 1% wt
% T-CNF	0	25	50	75	100
Recovery time (s)	3.9 ± 0.5	4.0 ± 0.9	13.8 ± 1.8	37.8 ± 2.2	44.2 ± 2.2
Recovery (%)	91.7 ± 13.1	94.0 ± 2.7	88.1 ± 0.4	81.0 ± 1.0	79.6 ± 6.6
Viscosity (mPa.s) step 1	43 ± 14	63 ± 2	190 ± 5	746 ± 20	1235 ± 103
Viscosity (mPa.s) step 2	2 ± 1	5 ± 1	10 ± 1	20 ± 1	25 ± 1
Viscosity (mPa.s) step 3	38 ± 7	59 ± 2	167 ± 5	604 ± 13	981 ± 99

In previous work, it was established that the rheological behaviour is predominantly dictated by the T-CNF in the T-CNF/Ag NWs inks [22, 46]. For this reason, the different parameters extracted were drawn against the proportion of T-CNF in the ink (**Fig. 3**).

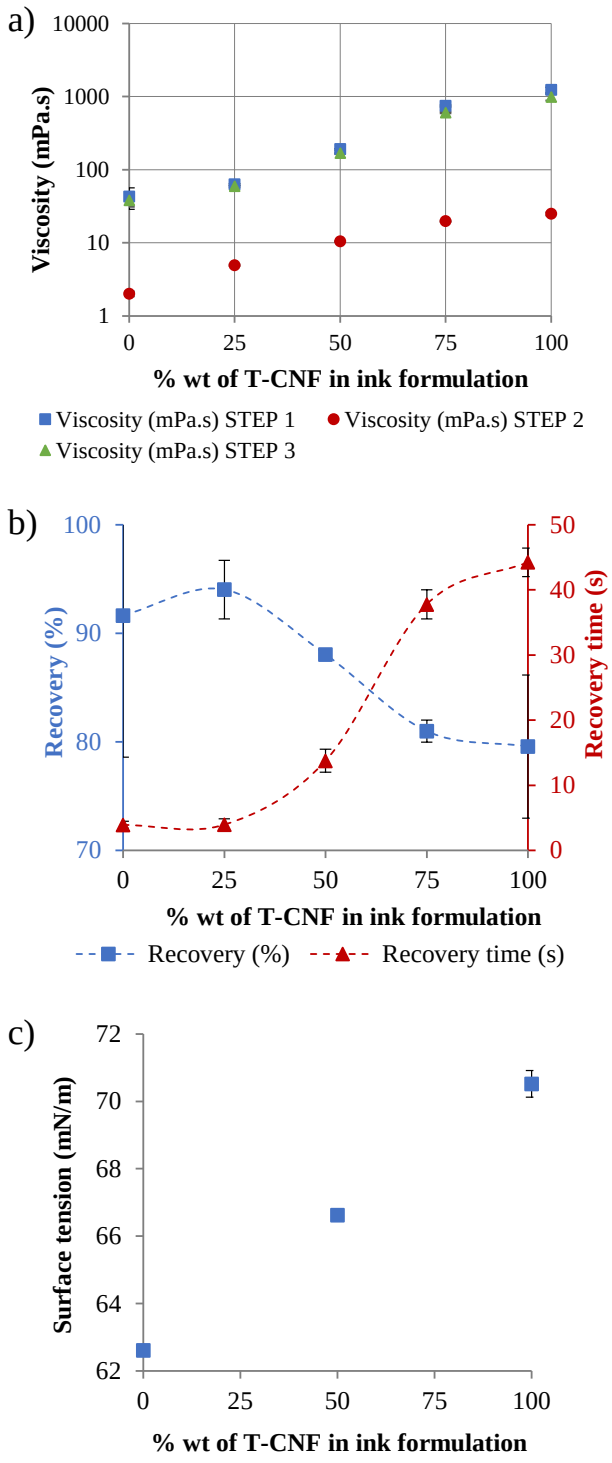

337

338 ***Fig. 3*** *Rheological parameters extracted from the 3-step model compared to the T-CNF content*

339 *of the inks with a) the viscosity (mPa.s) at the end of each step, b) the recovery (%) and the*

340 *recovery time (s) and other ink properties with c) measured surface tension (mN.m^{-1})*

Firstly, and as expected, all the different inks prepared exhibit strong shear shinning behaviour [25, 47] (**Fig. 3a**). This behaviour is essential for the formulated ink to properly flow ahead of the squeegee and then through the mesh opening to cover the desired surface.

The recovery (%) is dependent on the T-CNF concentration: the higher the T-CNF concentration the lower the recovery (**Fig. 3b**), which may be due to a permanent disruption of the more entangled network. The recovery time was also impacted by the ink composition (**Fig. 3b**). The recovery time indeed increase with an increasing T-CNF content. It is below 10 s from 0 to 50% wt of T-CNF in the ink, and reaches 44.2 s for T-CNF 1%. The same plausible explanation applies for both parameters: the higher amount of T-CNF, the more entangled and denser the network, and so the permanent the disruption of the network is by the high shear step. This proposed mechanism is represented schematically in **Fig. 4**. For the formulation at low CNF content, the high shear step orients the T-CNF and Ag NWs yet does not significantly impact the network structure because of a low entanglement factor. On the other hand, regarding the formulation at high T-CNF content, not only does the high shear step align the nanoparticles but could also break the pre-formed entangled network and disrupt any uncomplete percolation pathway.

In an attempt to analyse this, the entanglement of the system could also be assessed by comparing the concentration of raw materials in the different ink formulation to the estimated critical percolation threshold where particulate contact occurs. By assuming a cellulose density of 1.5 g.cm^{-3} and silver density of 10.5 g.cm^{-3} and using the estimated dimensions of the T-CNF and Ag NWs the critical percolation threshold can be calculated using equation **6** [48, 49]:

$$\varphi_c = 0.7\frac{d}{L} \quad (\mathbf{6})$$

Where φ_c is the estimated critical percolation threshold, d and L are respectively the diameter and length of the raw materials. The estimated critical percolation threshold was then compared

to the volume concentration for each of the raw materials in this ink (**Table 3**). This shows the fact that the systems are not fully percolated at the concentration and so consistent with the previous proposed mechanism. Furthermore, it is important to keep in mind that this estimation of the entanglement and crowdedness does not consider the effect of electrostatic repulsion, which is a critical parameter when working with highly charged T-CNF materials. Indeed, if highly charged CNF such as T-CNF are not expected to display major flocculation behaviour, the impact of high shear rate on the T-CNF network is still important [50]. High shear rate is expected to break down the gel structure and lead to the fibres alignment, deformation and gradient of fibres concentration at the microscale level [47, 51]. Beyond the T-CNF, the impact of the Ag NWs and their equilibrium with silver ions is unclear, but could also play a role in the charged structure of the network [25, 52]. In order to fully understand the complex hybrid systems made of T-CNF and Ag NWs, an interesting path to explore in the future could be to work on better modelling the networks formed, by considering the difference in flexibility/rigidity of the raw materials, as well as adding a rotational component to their orientation under shear [53, 54].

Table 3 Estimation of the critical percolation threshold compared to the volume concentration (% vol) of T-CNF and Ag NWs in the ink formulations

	% wt	% vol	φc (% vol)
T-CNF	0.25	0.17	1.89
	0.5	0.33	
	0.75	0.50	
	1	0.67	
Ag NWs	0.25	0.02	0.18
	0.5	0.05	
	0.75	0.07	
	1	0.10	

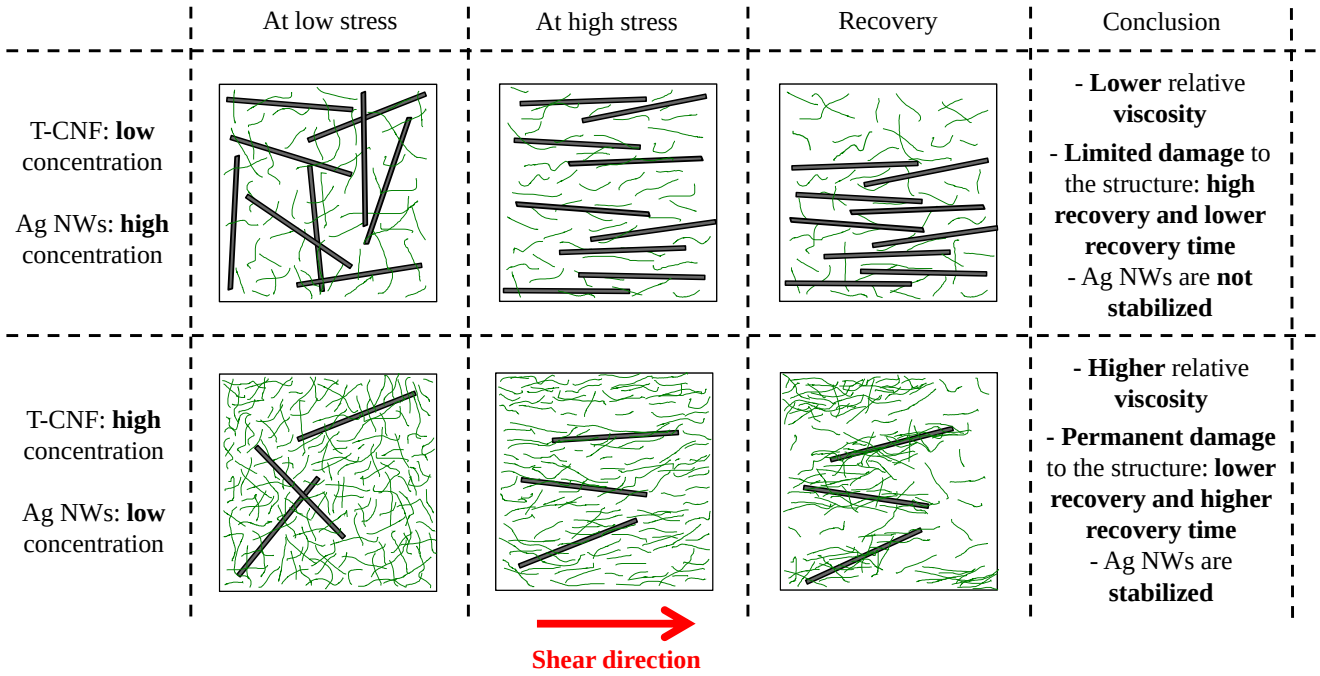

382

383 ***Fig. 4*** *Schematic representation (cross-section) of two separate formulation (high or low ratio*
384 *of T-CNF/Ag NWs) under different situation (low or high shear stress, recovery) and impact on*
385 *its network*

386 For screen printing, the optimum target for the recovery would be close to 100% to allow a
387 maximum print resolution or stabilisation of a coated film. The time necessary for the ink to
388 recover its viscosity is also an important parameter. The ideal situation would be to have a
389 recovery fast enough to achieve a homogenous levelling (> ca. 10 s) but not too long to avoid
390 extensive slumping (< ca. 200 s) [22, 55, 56]. All the different formulations display a high
391 enough recovery (%) for printing with high resolution. However, in the 0 to 50% of T-CNF
392 range, the recovery times are small (< 10 s) and these characteristic times could be too small
393 for an even levelling of the ink on the substrate to provide a smooth surface [22, 55]. This
394 suggests that the adequate rheological conditions are a higher mass content ink with a T-CNF
395 content higher than 50% wt. The increasing recovery times with the increasing T-CNF content
396 is promising because a higher mass content ink is usually used in screen-printing applications.
397 Classically, in the field of functional printing and coating, another parameter to consider for an

optimal deposition is the substrate/ink interaction. It was found out that the inks prepared (**Fig. 3c**) presents a relatively high surface tension (ranging from 62 to 71 $mN.m^{-1}$) compared to the surface energy of the PET substrate (*ca.* 40 $mN.m^{-1}$). Although this study is aimed at the rheological behaviour of the active inks composed of T-CNF and Ag NWs, this energy difference between inks and substrate could lead to unsatisfactory substrate/ink interaction and especially poor wetting and spreading of the ink on the substrate, and so potential dewetting printing defects.

As discussed above, T-CNF has a strong impact on viscosity, and in order to fit more closely with the screen-printing process requirements, the concentration of T-CNF was fixed at 1.66% wt, and a total mass of 2.5 %wt with a 2:1 ratio was selected. Previous work on similar systems has shown the positive impact of the addition of water-soluble polymer such as hydroxypropyl methylcellulose (HPMC) [22], mainly on the recovery time and the viscoelastic properties of the formulated inks. So, different amount (0, 3, 5 and 8% wt) were added in the selected T-CNF/Ag NWs blend.

The same three step rheological model was applied to the HPMC formulations, and the same parameters linked to viscosity and recovery were extracted (**Table *4***). The viscosity *versus* time graphs can be found in the electronic supplementary material (**Fig. SI 3** and **Fig. SI 4**). The reference 0% HPMC (=T-CNF/Ag NWs 2.5% wt 2:1) displays a recovery (72.4%) slightly higher than the T-CNF 1.66% wt formulation (64.7%) showing that the addition of Ag NWs also impacts the recovery (%), whereas the recovery time was relatively similar for both formulations (respectively 39.6 s for 0% HPMC and 37.3 s for T-CNF 1.66% wt).

The viscosity drastically increases with the concentration of HPMC, going from 8.2 Pa.s for HPMC 0% to 57.4 Pa.s for HPMC 8%, due to the thickening effect of the water-soluble cellulose derivative [22]. With an increasing amount of HPMC, the recovery (%) drops from

72.4% for HPMC 0% to 59.2% for HPMC 3%. It is not too much impacted for HPMC 5% and HPMC 8% (respectively 59.1 and 65.5%). The recovery time however decreases with an increasing content of HPMC, reaching 13.6 s for 8% HPMC compared to 29.2 for 5% HPMC or 33.6 for 3% HPMC.

The recovery parameters (time and %) are promising for 0% HPMC but its viscosity is in the low range of what is classically expected for screen-printing inks. The 5% HPMC formulation is selected to be a good compromise between recovery and viscosity parameters.

Table 4 Values of recovery time (s), recovery (%) and viscosity (mPa.s) extracted from the 3-step model for the formulations with different HPMC content compared to T-CNF 1.66% wt

	T-CNF 1.66%	**0% HPMC**	**3% HPMC**	**5% HPMC**	**8% HPMC**
Recovery time (s)	40.4	39.6	33.6	29.2	13.6
Recovery (%)	64.7	72.4	59.2	59.1	65.5
Viscosity (mPa.s) step 1	8691	8209	17229	29341	57426
Viscosity (mPa.s) step 2	10	72	293	795	1057
Viscosity (mPa.s) step 3	5627	5945	10193	17344	37607

3.2. Additive use and impact on print quality

The formulation with different content of HPMC were printed and the resulting patterns can be found in **Fig. 5a**, **b**, **c** and **d**. The print quality is greatly enhanced visually with the addition of 5% wt or 8% wt of HPMC. This is mostly consistent with the previous rheological parameters extracted from the experiments but not entirely, showing that the usual rheological test can only give a general guidance for provision of the print quality.

For a quantitative comparison, the quality of the print was estimated by image analysis. Adding HPMC reduces the statistical dispersion of the grey histogram and the graphs are shifted from the black background to a higher intensity meaning a better coverage of the surface and less mottling defect that makes the substrate appear under the print (**Fig. 5e**). There is not much difference between the prints at 5 and 8% of HPMC and this was confirmed by the standard deviation of the grey histogram distribution (**Table 5**).

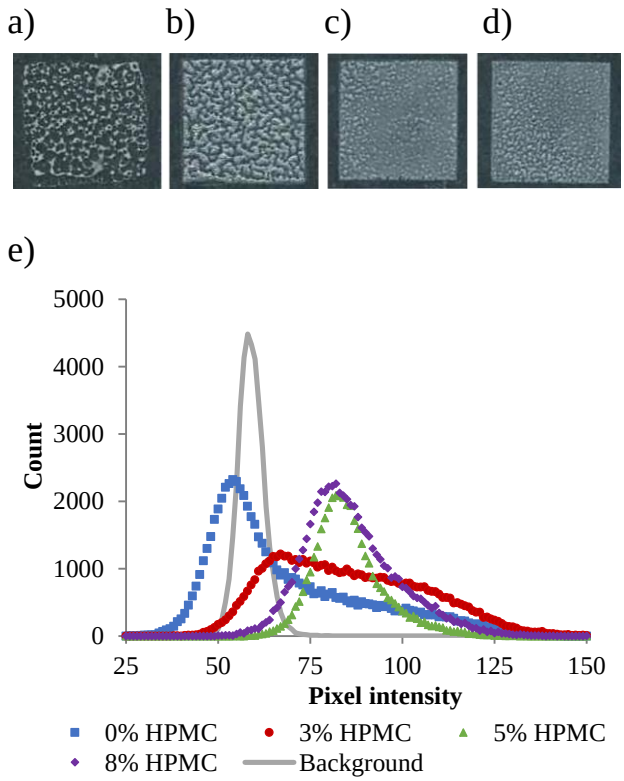

Fig. 5 *Quality assessment of the printed square on PET substrate with T-CNF/Ag NWs 2.5% wt 2:1 and different amount of HPMC with visual pictures for a) 0% wt, b) 3% wt, c) 5% wt and d) 8% wt and grey histogram distribution for the different formulation printed and comparison with the black background*

The topography of the print was also assessed by white light interferometry by measuring the thickness and surface roughness of the prints (**Table 5**). For the reference formulation without any HPMC (0% HPMC), the quality of the print was not sufficient to measure reliable

topological parameters. This could be due to poor wetting dynamics which seems to be enhanced by the addition of HPMC. For all other samples, the quality was deemed to be sufficient for reliable measurements. However, the issue of homogeneous spreading and the presence of defects even for high content of HPMC is reflected in the high standard deviation obtained for thickness and roughness measurements. For 3% HPMC, 5% HPMC and 8% HPMC, the measured dry thickness is less than 1 µm which might be surprising for screen printing but consistent with the very low mass content of the ink compared to conventional screen-printing inks. The measured thicknesses are increasing with an increasing content of HPMC and range from 269 to 811 nm. For all samples the surface roughness is relatively similar for each sample. Due to the print quality, the transparency measurements were not reliable for the 0% HPMC. The pattern transmittance was measured at 75.2, 73.3 and 68.0%, respectively for 3% HPMC, 5% HPMC and 8% HPMC. There is a significant decrease in the transparency after printing, when compared to the PET substrate value, measured at 89.8 ± 1.4%. However, the final values reached are still relatively high and not very far from packaging targets, where a transparency value of 80% is an accepted guideline. The materials produced in this study are then considered as transparent enough for the developed solution to be used in active packaging application.

Table 5 *Characterization of the prints as function of the HPMC content in the ink with grey histogram standard deviation, thickness (nm), surface roughness (nm) and transparency (%) (N/A= not applicable)*

HPMC content (%)	0	3	5	8
Grey histogram standard deviation	20.8	20.2	9.6	12.7
Thickness (nm)	N/A	269 ± 138	622 ± 140	811 ± 276
Surface Roughness (*Sa*, nm)	N/A	450 ± 106	482 ± 134	549 ± 137
Transparency (T550nm, %)	N/A	75.2 ± 1.1	73.3 ± 0.9	68.0 ± 1.9

Finally, the HPMC 0% and HPMC 8% prints were tested against E. Coli bacterial contamination using the AATCC TM100-1998 standard designed for active surfaces (**Fig. 6a**). This test is adapted for contact active surface and is performed by drop-casting a bacterial suspension (know volume and known concentration) on top of the tested surface. After 24 hours of contact in an incubator (37°C, 100 RPM), the bacterial suspension is recovered, numbered and compared with the starting concentration. On the **Fig. 6a**, the horizontal line represents the starting concentration and the histograms represent the final concentration of the bacterial suspension after contact with either the PET reference film (untreated) and printed samples HPMC 0% and HPMC 5%. The antibacterial activity was calculated comparing the bacterial concentration at the end of the test, between the PET reference and the different samples.

Despite the low thickness of the deposited layers, the prints present a bactericidal activity toward E. Coli with a calculated antibacterial activity of 81.8% and 67.4% for HPMC 0% and HPMC 5% respectively. As previously described, the print quality is greatly enhanced from HPMC 0 to HPMC 5% and only a small loss in the antibacterial activity is registered between the two formulations, which probably corresponds to a deeper entrapment of the Ag NWs due to the HPMC addition and consequent lower accessibility and lower silver ions release (**Fig. 6b**). This is a significant result that proves the versatility of the formulation that can be adapted

to fit the process requirements, even at a large concentration of additives (5% wt) compared to the concentration of the antibacterial silver nanowires (0.84% wt). The high standard deviation of **Fig. 6a** can be attributed to the heterogenous surface due to the printing defects.

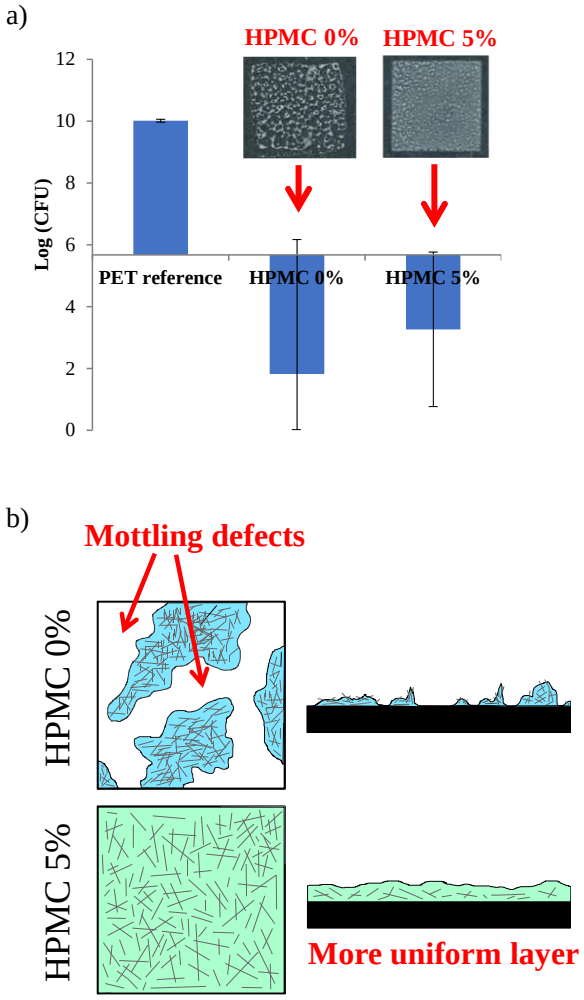

Fig. 6 *a) Qualitative analysis of the antibacterial activity of PET reference, HPMC 0% and HPMC 5% samples, using AATCC TM100-1998 standard vs E. Coli with results expressed in log of colony forming units (log CFU) and b) schematic representation of HPMC 0% and HPMC 5% and the benefits of adding HPMC into the ink formulation*

4. Conclusion

The rheological properties of ink formulations based on TEMPO-oxidised cellulose nanofibrils and silver nanowires were investigated in a systematic step-by-step manner. The viscosity and thixotropic behaviour of low-solid content inks were found to be highly dependent on the formulation and higher content screen-printing inks were then prepared based on the optimal formulation. Hydroxypropyl methylcellulose was included as an additive which improved the print quality and the rheological properties of the mixture were investigated in a similar manner. The quality of the print (image analysis, surface roughness and thickness) were correlated to the rheological findings and the antibacterial activity of the prints was established, which proves the potential application to use such a formulation for patterned antibacterial packaging applications. The possibility to introduce localized antibacterial pattern is interesting for all sorts of applications (food or medical packaging lids and seals for example) and promotes materials economy as well as easily tailored antibacterial solution when compared to full surface deposition.

Acknowledgements

This research was supported LabEx Tec 21 (Grant agreement No. ANR-11-LABX-0030). This research was made possible thanks to the facilities of the TekLiCell platform funded by the Région Rhône-Alpes (ERDF: European regional development fund). Authors want to thank Cécile Sillard and Eva Pasquier from Grenoble INP Pagora for the help with AFM and TEM imaging.

Conflicts of interest

There are no conflicts to declare.

Electronic Supplementary Information

The AFM images, as well as the details of the 3-step rheological model (viscosity *versus* time graphs) applied to the different formulation can be found in the Electronic Supplementary Information.

References

1. Yildirim S, Röcker B, Pettersen MK, et al (2018) Active Packaging Applications for Food. Comprehensive Reviews in Food Science and Food Safety 17:165–199. https://doi.org/10.1111/1541-4337.12322

2. Tang S, Zheng J (2018) Antibacterial Activity of Silver Nanoparticles: Structural Effects. Advanced Healthcare Materials 7:1701503. https://doi.org/10.1002/adhm.201701503

3. Li L, Zhao C, Zhang Y, et al (2017) Effect of stable antimicrobial nano-silver packaging on inhibiting mildew and in storage of rice. Food Chemistry 215:477–482. https://doi.org/10.1016/j.foodchem.2016.08.013

4. Wu Z, Huang X, Li Y-C, et al (2018) Novel chitosan films with laponite immobilized Ag nanoparticles for active food packaging. Carbohydrate Polymers 199:210–218. https://doi.org/10.1016/j.carbpol.2018.07.030

5. Fahad S, Yu H, Wang L, et al (2019) Recent progress in the synthesis of silver nanowires and their role as conducting materials. J Mater Sci 54:997–1035. https://doi.org/10.1007/s10853-018-2994-9

6. Kaimlová M, Nemogová I, Kolářová K, et al (2019) Optimization of silver nanowire formation on laser processed PEN: Surface properties and antibacterial effects. Applied Surface Science 473:516–526. https://doi.org/10.1016/j.apsusc.2018.12.185

7. Zhang Z, Wu Y, Wang Z, et al (2017) Electrospinning of Ag Nanowires/polyvinyl alcohol hybrid nanofibers for their antibacterial properties. Materials Science and Engineering: C 78:706–714. https://doi.org/10.1016/j.msec.2017.04.138

8. Mirjalili SH, Nateghi MR, Kalantari-Fotooh F (2020) Preparation of silver nanowire/expanded polytetrafluoroethylene and polypropylene nanocomposites via all solution process method for antibacterial applications. The Journal of The Textile Institute 111:139–147. https://doi.org/10.1080/00405000.2019.1627981

9. Lei J, Zhou L, Tang Y, et al (2017) High-Strength Konjac Glucomannan/Silver Nanowires Composite Films with Antibacterial Properties. Materials 10:524. https://doi.org/10.3390/ma10050524

10. Kiran Shahzadi, Wu L, Ge X, et al (2016) Preparation and characterization of bio-based hybrid film containing chitosan and silver nanowires. Carbohydrate Polymers 137:732–738. https://doi.org/10.1016/j.carbpol.2015.11.012

11. Satoungar MT, Fattahi S, Azizi H, Mehrizi MK (2018) Electrospinning of Polylactic Acid/silver nanowire biocomposites: Antibacterial and electrical resistivity studies. Polymer Composites 39:E65–E72. https://doi.org/10.1002/pc.24241

12. Xu Y, Li S, Yue X, Lu W (2017) Review of Silver Nanoparticles (AgNPs)-Cellulose Antibacterial Composites. BioResources 13:2150-2170–2170. https://doi.org/10.15376/biores.13.1.Xu

13. Uddin KMA, Orelma H, Mohammadi P, et al (2017) Retention of lysozyme activity by physical immobilization in nanocellulose aerogels and antibacterial effects. Cellulose 24:2837–2848. https://doi.org/10.1007/s10570-017-1311-0

14. Yan J, Abdelgawad AM, El-Naggar ME, Rojas OJ (2016) Antibacterial activity of silver nanoparticles synthesized In-situ by solution spraying onto cellulose. Carbohydrate Polymers 147:500–508. https://doi.org/10.1016/j.carbpol.2016.03.029

15. Saarinen JJ, Remonen T, Tobjörk D, et al (2017) Large-Scale Roll-to-Roll Patterned Oxygen Indicators for Modified Atmosphere Packages. Packaging Technology and Science 30:219–227. https://doi.org/10.1002/pts.2295

16. Wen J, Huang S, Jia L, et al (2019) Visible Colorimetric Oxygen Indicator Based on Ag-Loaded TiO2 Nanotubes for Quick Response and Real-Time Monitoring of the Integrity of Modified Atmosphere Packaging. Advanced Materials Technologies 4:1900121. https://doi.org/10.1002/admt.201900121

17. Tan EL, Ng WN, Shao R, et al (2007) A Wireless, Passive Sensor for Quantifying Packaged Food Quality. Sensors 7:1747–1756. https://doi.org/10.3390/s7091747

18. Yousefi H, Ali MM, Su H-M, et al (2018) Sentinel Wraps: Real-Time Monitoring of Food Contamination by Printing DNAzyme Probes on Food Packaging. ACS Nano 12:3287–3294. https://doi.org/10.1021/acsnano.7b08010

19. Koga H, Saito T, Kitaoka T, et al (2013) Transparent, Conductive, and Printable Composites Consisting of TEMPO-Oxidized Nanocellulose and Carbon Nanotube. Biomacromolecules 14:1160–1165. https://doi.org/10.1021/bm400075f

20. Nechyporchuk O, Yu J, Nierstrasz VA, Bordes R (2017) Cellulose Nanofibril-Based Coatings of Woven Cotton Fabrics for Improved Inkjet Printing with a Potential in E-Textile Manufacturing. ACS Sustainable Chem Eng 5:4793–4801. https://doi.org/10.1021/acssuschemeng.7b00200

21. El Baradai O, Beneventi D, Alloin F, et al (2016) Microfibrillated Cellulose Based Ink for Eco-Sustainable Screen Printed Flexible Electrodes in Lithium Ion Batteries. Journal of Materials Science & Technology 32:566–572. https://doi.org/10.1016/j.jmst.2016.02.010

22. Hoeng F, Denneulin A, Reverdy-Bruas N, et al (2017) Rheology of cellulose nanofibrils/silver nanowires suspension for the production of transparent and conductive electrodes by screen printing. Applied Surface Science 394:160–168. https://doi.org/10.1016/j.apsusc.2016.10.073

23. Espinosa E, Filgueira D, Rodríguez A, Chinga-Carrasco G (2019) Nanocellulose-Based Inks—Effect of Alginate Content on the Water Absorption of 3D Printed Constructs. Bioengineering 6:65. https://doi.org/10.3390/bioengineering6030065

24. Syrový T, Maronová S, Kuberský P, et al (2019) Wide range humidity sensors printed on biocomposite films of cellulose nanofibril and poly(ethylene glycol). Journal of Applied Polymer Science 136:47920. https://doi.org/10.1002/app.47920

25. Hubbe MA, Tayeb P, Joyce M, et al (2017) Rheology of Nanocellulose-rich Aqueous Suspensions: A Review. BioResources 12:9556–9661

601 26. Naderi A, Lindström T (2016) A comparative study of the rheological properties of three
602 different nanofibrillated cellulose systems. Nordic Pulp & Paper Research Journal
603 31:354–363. https://doi.org/10.3183/npprj-2016-31-03-p354-363

604 27. Saito T, Nishiyama Y, Putaux J-L, et al (2006) Homogeneous suspensions of
605 individualized microfibrils from TEMPO-catalyzed oxidation of native cellulose.
606 Biomacromolecules 7:1687–1691. https://doi.org/10.1021/bm060154s

607 28. Alves L, Ferraz E, Lourenço AF, et al (2020) Tuning rheology and aggregation behaviour
608 of TEMPO-oxidised cellulose nanofibrils aqueous suspensions by addition of different
609 acids. Carbohydrate Polymers 237:116109.
610 https://doi.org/10.1016/j.carbpol.2020.116109

611 29. Fukuzumi H, Tanaka R, Saito T, Isogai A (2014) Dispersion stability and aggregation
612 behavior of TEMPO-oxidized cellulose nanofibrils in water as a function of salt addition.
613 Cellulose 21:1553–1559. https://doi.org/10.1007/s10570-014-0180-z

614 30. Calabrese V, Muñoz-García JC, Schmitt J, et al (2019) Understanding heat driven gelation
615 of anionic cellulose nanofibrils: Combining saturation transfer difference (STD) NMR,
616 small angle X-ray scattering (SAXS) and rheology. Journal of Colloid and Interface
617 Science 535:205–213. https://doi.org/10.1016/j.jcis.2018.09.085

618 31. Silva MA da, Calabrese V, Schmitt J, et al (2018) Alcohol induced gelation of TEMPO-
619 oxidized cellulose nanofibril dispersions. Soft Matter 14:9243–9249.
620 https://doi.org/10.1039/C8SM01815D

621 32. Quennouz N, Hashmi SM, Choi HS, et al (2015) Rheology of cellulose nanofibrils in the
622 presence of surfactants. Soft Matter 12:157–164. https://doi.org/10.1039/C5SM01803J

623 33. Martins NCT, Freire CSR, Pinto RJB, et al (2012) Electrostatic assembly of Ag
624 nanoparticles onto nanofibrillated cellulose for antibacterial paper products. Cellulose
625 19:1425–1436. https://doi.org/10.1007/s10570-012-9713-5

626 34. Hemmati S, Barkey DP, Gupta N (2016) Rheological behavior of silver nanowire
627 conductive inks during screen printing. J Nanopart Res 18:249.
628 https://doi.org/10.1007/s11051-016-3561-4

629 35. Tanaka R, Saito T, Hondo H, Isogai A (2015) Influence of Flexibility and Dimensions of
630 Nanocelluloses on the Flow Properties of Their Aqueous Dispersions. Biomacromolecules
631 16:2127–2131. https://doi.org/10.1021/acs.biomac.5b00539

632 36. Foster EJ, Moon RJ, Agarwal UP, et al (2018) Current characterization methods for
633 cellulose nanomaterials. Chem Soc Rev 47:2609–2679.
634 https://doi.org/10.1039/C6CS00895J

635 37. Schindelin J, Arganda-Carreras I, Frise E, et al (2012) Fiji: an open-source platform for
636 biological-image analysis. Nat Methods 9:676–682. https://doi.org/10.1038/nmeth.2019

637 38. Schneider CA, Rasband WS, Eliceiri KW (2012) NIH Image to ImageJ: 25 years of image
638 analysis. Nat Methods 9:671–675. https://doi.org/10.1038/nmeth.2089

639 39. Besbes I, Alila S, Boufi S (2011) Nanofibrillated cellulose from TEMPO-oxidized
640 eucalyptus fibres: Effect of the carboxyl content. Carbohydrate Polymers 84:975–983.
641 https://doi.org/10.1016/j.carbpol.2010.12.052

642 40. Benhamou K, Dufresne A, Magnin A, et al (2014) Control of size and viscoelastic
643 properties of nanofibrillated cellulose from palm tree by varying the TEMPO-mediated
644 oxidation time. Carbohydrate Polymers 99:74–83.
645 https://doi.org/10.1016/j.carbpol.2013.08.032

646 41. Neidert M, Zhang W, Zhang D, Kipka A (2008) Screen-printing simulation study on solar
647 cell front side AG paste. In: 2008 33rd IEEE Photovoltaic Specialists Conference. pp 1–4

648 42. AATCC standard (1998) TM100 - Test Method for Antibacterial Finishes on Textile
649 Materials: Assessment of Antibactrial Textile. AATCC, Research Triangle Park, NC

650 43. Shinoda R, Saito T, Okita Y, Isogai A (2012) Relationship between Length and Degree of
651 Polymerization of TEMPO-Oxidized Cellulose Nanofibrils. Biomacromolecules 13:842–
652 849. https://doi.org/10.1021/bm2017542

653 44. Barnes HA (1997) Thixotropy—a review. Journal of Non-Newtonian Fluid Mechanics
654 70:1–33. https://doi.org/10.1016/S0377-0257(97)00004-9

655 45. Shao Y, Chaussy D, Grosseau P, Beneventi D (2015) Use of Microfibrillated
656 Cellulose/Lignosulfonate Blends as Carbon Precursors: Impact of Hydrogel Rheology on
657 3D Printing. Ind Eng Chem Res 54:10575–10582.
658 https://doi.org/10.1021/acs.iecr.5b02763

659 46. Spieser H, Denneulin A, Deganello D, et al (2020) Cellulose nanofibrils and silver
660 nanowires active coatings for the development of antibacterial packaging surfaces.
661 Carbohydrate Polymers 240:116305. https://doi.org/10.1016/j.carbpol.2020.116305

662 47. Lasseuguette E, Roux D, Nishiyama Y (2008) Rheological properties of microfibrillar
663 suspension of TEMPO-oxidized pulp. Cellulose 15:425–433.
664 https://doi.org/10.1007/s10570-007-9184-2

665 48. Moberg T, Sahlin K, Yao K, et al (2017) Rheological properties of nanocellulose
666 suspensions: effects of fibril/particle dimensions and surface characteristics. Cellulose
667 24:2499–2510. https://doi.org/10.1007/s10570-017-1283-0

668 49. Xu X, Liu F, Jiang L, et al (2013) Cellulose Nanocrystals vs. Cellulose Nanofibrils: A
669 Comparative Study on Their Microstructures and Effects as Polymer Reinforcing Agents.
670 ACS Appl Mater Interfaces 5:2999–3009. https://doi.org/10.1021/am302624t

671 50. Nechyporchuk O, Belgacem MN, Pignon F (2016) Current Progress in Rheology of
672 Cellulose Nanofibril Suspensions. Biomacromolecules 17:2311–2320.
673 https://doi.org/10.1021/acs.biomac.6b00668

674 51. Martoïa F, Perge C, Dumont PJJ, et al (2015) Heterogeneous flow kinematics of cellulose
675 nanofibril suspensions under shear. Soft Matter 11:4742–4755.
676 https://doi.org/10.1039/C5SM00530B

677 52. Fall AB, Lindström SB, Sprakel J, Wågberg L (2013) A physical cross-linking process of
678 cellulose nanofibril gels with shear-controlled fibril orientation. Soft Matter 9:1852–1863.
679 https://doi.org/10.1039/C2SM27223G

680 53. Rosén T, Hsiao BS, Söderberg LD Elucidating the Opportunities and Challenges for
681 Nanocellulose Spinning. Advanced Materials n/a:2001238.
682 https://doi.org/10.1002/adma.202001238

683 54. Schmid CF, Klingenberg DJ (2000) Mechanical Flocculation in Flowing Fiber
684 Suspensions. Phys Rev Lett 84:290–293. https://doi.org/10.1103/PhysRevLett.84.290

685 55. Faddoul R, Reverdy-Bruas N, Blayo A (2012) Formulation and screen printing of water
686 based conductive flake silver pastes onto green ceramic tapes for electronic applications.
687 Materials Science and Engineering: B 177:1053–1066.
688 https://doi.org/10.1016/j.mseb.2012.05.015

689 56. Elen K, Penxten H, Nagels S, et al (2018) Screen-printing of flexible semi-transparent
690 electrodes and devices based on silver nanowire networks. Nanotechnology 29:425201.
691 https://doi.org/10.1088/1361-6528/aad74d